Evolution of Fe environments and phase composition during mechanical amorphization of $Fe_{70}Zr_{30}$ and $Fe_{70}Nb_{30}$ alloys

A. F. Manchón-Gordón, J. J. Ipus, J. S. Blázquez*, C. F. Conde, A. Conde

Dpto. Física de la Materia Condensada, ICMSE-CSIC, Universidad de Sevilla, P.O. Box 1065, 41080 Sevilla, Spain
The corresponding author e-mail: jsebas@us.es

ABSTRACT: Amorphous Fe-Zr and Fe-Nb alloys with 70 at. % Fe have been prepared by ball milling a mixture of elemental powders. The combination of Mössbauer spectroscopy, X-ray diffraction, scanning electron microscopy and differential scanning calorimetry techniques supplies detailed information about the composition as well as microstructural parameters of remaining crystalline and amorphous phases developed during milling. Detailed analysis of the Fe environments allows us to distinguish Fe atoms in paramagnetic sites between those incorporated to crystalline Zr or Nb rich phases and those Fe atoms in amorphous phase.

KEYWORDS: mechanical amorphization, mechanical alloying, amorphous alloys

1.   INTRODUCTION

Advanced materials can be defined as those that represent superior properties over the traditional materials for demanding applications. Typically, progress on improving the properties of these materials is given thanks to the systematic synthesis and control of the structure of the materials [1] processing them under non-equilibrium conditions [2]. Among the different processes in commercial use, mechanical alloying (MA) [2], plasma processing [3] or rapid solidification from the liquid state [4] can be signed.

MA technique, originally developed to produce oxide-dispersion strengthened nickel and iron base superalloys for applications in the aerospace industry [5], has a unique

capability of producing thermodynamically disfavored reactions and destabilizing equilibrium systems [2]. In fact, the large diversity of metastable systems that can be produced by MA, including amorphous alloys, supersaturated solid solutions or metastable intermetallics, makes this technique to be present in many research fields [2, 6]. Generally, high energetic milling of alloys leads to the formation of a nanocrystalline structure and, for some compositions, to amorphization [2].

Iron-based systems are among the most suitable materials for studying the mechanical milling as a process and the properties of the final products. The cheap character of this element makes it desirable and ubiquitous in any technological field. The magnetic nature of many compounds of iron significantly increases the amount of information that can be obtained for these systems. Moreover, the existence of a Mössbauer isotope, ^{57}Fe, in a non-negligible natural abundance [7] makes possible the study of hyperfine interactions of Fe-compounds. Therefore, all this leads to a more comprehensive understanding of the material. Particularly, the Fe-Zr alloys present extremely different magnetic properties depending on Fe content [8, 9] and the local atomic order [10], as well as a wide range of the existence of the amorphous phase, Fe_xZr_{100-x} ($20 \leq x \leq 93$ at. %) [11]. In the case of the Fe-Nb alloys, although still some research is needed to determine a complete phase diagram [12], amorphous phase is found in a wide compositional range [13, 14]. These phases show interesting peculiarities due to singular aspects of their nanostructures [15]. In a previous study [16] we used $Fe_{70}Zr_{30}$ and $Fe_{70}Nb_{30}$ (at. %) compositions to show the validity of the cubic law [17] that correlates the progress of milling with the frequency of the mill.

Microstructural and compositional characterization of amorphous structures is an essential point to optimize technological properties in which they are based on. However, this characterization is critical for nanoscale systems, for which the

characteristic size to be studied is so tiny that could presumably only be attainable to nanoprobe techniques. Otherwise, due to the extremely local character of atom-scale techniques, statistics using tiny probes are not straightforward. For example, in the analysis of a nanocrystal using atom probe, the sensitivity in the composition is not as good as for systems with a well-defined flat interface. Assuming a 5 nm sphere, the range not affected by the surface geometry is limited to a cube of $5/\sqrt{3}$ nm in size. In the case of a bcc-Fe phase, this implies a length of only ~10 unit cells. On the other hand, methods based on global techniques (X-ray diffraction, Mössbauer spectroscopy, etc.) present the advantage of a much better statistics to obtain average values and are experimental techniques accessible to most of the scientific community. In fact, the capability of Mössbauer spectroscopy to analyze nanoscale systems have been pointed out, particularly when combining with other techniques, such as X-ray diffraction [18, 19].

Currently, there are many investigations on amorphous Fe-Zr and Fe-Nb phases obtained by different techniques and on the structural analysis of the products of mechanical alloying in these systems [10, 14, 20-24]. However, no systematic study of the composition of both amorphous and remnant bcc nanocrystals in Fe-based supersaturated solid solutions have been undertaken. In our case, we combined XRD and Mössbauer data to estimate the compositions of nanocrystals in FeNbB supersaturated solid solution [19]. It is worth mentioning that the knowledge of the composition of the different phases is very helpful to propose accurate models to describe the behavior of any physical system. In the present work, amorphous Fe-Zr and Fe-Nb alloys with 70 at. % Fe have been prepared using mechanical alloying. The microstructural evolution of both alloys was followed by Mössbauer spectroscopy, X-ray diffraction, scanning electron microscopy and differential scanning calorimetry. The

combination of these techniques supplies very detailed information about the composition of nanocrystals and the amorphous phase developed during mechanical alloying. Moreover, from the evolution of the compositions of nanocrystals core it has been possible to estimate the interface thickness.

2.   EXPERIMENTAL

Fe-Zr and Fe-Nb alloys with 70 at. % Fe were prepared by ball milling of elemental powders mixture in a planetary mill Fritsch Pulverisette Vario 4 using hardened steel balls and steel vials. The initial powder mass was 30 g, the ball to powder ratio 10:1 and the ratio between the rotational speeds of the vials and the main disk -2. Continuous milling steps of 0.5 h were performed in Ar atmosphere and after selected times, approximately 0.2 g of sample was extracted in a Saffron Omega glove box with oxygen and humidity levels below 2 ppm under Ar atmosphere.

The microstructure was studied by X-ray diffraction (XRD) using Cu-Kα radiation in a Bruker D8 I diffractometer. Differential scanning calorimetry (DSC) was performed in a TA-Instruments Q600 SDT under nitrogen flow. The powder samples were pressed in silver capsules and a baseline was obtained using a standard Ag sample. Particle size distribution and morphology was studied by scanning electron microscopy (SEM) in secondary electrons mode performed in a Jeol 6460 LV microscope operated at 30 kV. The local environment of Fe atoms was analyzed by Mössbauer spectrometry (MS) in transmission geometry at room temperature (RT) using a ^{57}Co(Rh) source. Values of the hyperfine parameters were obtained by fitting with NORMOS program [25] and the isomer shift (*IS*) was quoted relative to the Mössbauer spectrum of an α-Fe foil at RT.

3. RESULTS and DISCUSSION

3.1. X-ray diffraction results

XRD patterns of $Fe_{70}Zr_{30}$ and $Fe_{70}Nb_{30}$ alloys after selected milling times are presented in figure 1. The amorphous phase of the as-milled samples is evidenced by a wide amorphous halo in samples milled for at least $t = 6$ and 9 h, for $Fe_{70}Zr_{30}$ and $Fe_{70}Nb_{30}$, respectively. XRD does not clearly show the expected displacement to lower angles of bcc Fe diffraction maxima that should indicate an increase of the lattice parameter, a, as Zr or Nb atoms become integrated into the bcc Fe(Zr) and Fe(Nb) solid solution, respectively, although a slight effect can be observed at short times. The bcc Fe maxima get broader as milling time increases due to the reduction of the crystal size and the increase of microstrains during milling. Peaks attributed to the hcp Zr and bcc Nb phases are only detected for short milling times ($t < 6$ and $t < 12$ h for $Fe_{70}Zr_{30}$ and $Fe_{70}Nb_{30}$, respectively).

The evolution of the amorphous phase with milling time was estimated from a deconvolution of the main X-ray peak to separate the (110) line of the α-Fe nanocrystals (narrow Lorentzian contribution) and the amorphous halo (broad Gaussian contribution). Therefore, the amorphous volume fraction can be estimated as the area of the Gaussian contribution (amorphous halo) divided by the whole area of the experimental diffraction peak. In the case of the $Fe_{70}Nb_{30}$ alloy, for short milling times ($t < 12$ h), it is necessary to take into account the contribution of the (110) peak of the bcc Nb nanocrystals.

Figure 2 shows the evolution of the crystal size, D, estimated from Scherrer's formula from the full width at half maximum of crystalline (110) diffraction peak, as a function of milling time for both alloys along with that of Nb phase for $Fe_{70}Nb_{30}$ alloy. Final D

of bcc-Fe type phase is clearly larger for $Fe_{70}Zr_{30}$ alloy, for which a stable value ~10 nm is rapidly achieved, meanwhile D continuously decreases down to ~5 nm for the Nb-containing alloy. The evolution of the lattice parameter of the α-Fe(X), being X=Zr, Nb, as a function of milling time is shown in figure 3. As commented above, the expected increase in lattice parameter is clearer for $Fe_{70}Nb_{30}$ than for $Fe_{70}Zr_{30}$ alloy. The position of the amorphous halo shifts to higher 2θ values as milling progresses (figure 4a). This indicates a contraction of the average metal-metal distance (figure 4b), which can be estimated as [26]:

$$\delta_{M-M} = \frac{5\lambda}{8\sin\theta} \tag{1}$$

where λ is the wavelength of the used radiation.

3.2. Differential scanning calorimetry results

In order to verify the formation of the amorphous structure, DSC curves of both studied alloys were recorded in non-isothermal regime. Figure 5 shows the DSC scans at 20 K/min of both studied samples after ~50 h of milling. All the features found in the curves are irreversible as they vanish in a second heating. The well-defined exothermic peaks around 950 and 1000 K for Zr and Nb containing alloys, respectively, correspond to crystallization of the amorphous phase. Previous deviations from baseline are ascribed to relaxation phenomena in agreement with the literature [9, 17]. The obtained values of the onset temperatures T_{onset} and peak temperatures T_{peak} of crystallization process are shown in Table 1. The values obtained for the $Fe_{70}Zr_{30}$ alloy are similar to those reported by Mishra et al. [9]. However, T_{onset} of powder samples are slightly higher than those obtained for ribbon samples [27]. In the case of the Nb containing alloy, the values obtained are close to those reported by El-Eskandarany et al. [22] for amorphous $Fe_{52}Nb_{48}$ alloy powder.

3.3.Scanning electron microscopy results

Microstructural modifications induced by milling can be followed from a direct comparison of the secondary electron images (figure 6) for the two studied alloys. These show the existence of agglomerates at early milling times (t =6 and 8.5 h for $Fe_{70}Zr_{30}$ and $Fe_{70}Nb_{30}$, respectively), meanwhile at longer milling times (t >22 h) almost spherical isolated powder particles are found. Although those agglomerates are present in both samples, for $Fe_{70}Nb_{30}$ the size of particles is larger and the number of particles per agglomerate is smaller than for $Fe_{70}Zr_{30}$ samples for equivalent milling times (e.g. after ~20 h milling, $Fe_{70}Nb_{30}$ alloy shows few tens of particles per agglomerate, meanwhile $Fe_{70}Zr_{30}$ shows few hundreds of particles per agglomerate). Insets of figure 6 show the corresponding grain size distribution histograms. The particle size after different milling times was obtained by averaging over a minimum of 50 particles for each sample. Particle size decreases with milling until 22 h, achieving sizes about d~12±4 and 33±13 μm for $Fe_{70}Zr_{30}$ and $Fe_{70}Nb_{30}$, respectively. After this time of milling, the particle size increases, finally reaching sizes about d~23±11 and 44±18 μm for $Fe_{70}Zr_{30}$ and $Fe_{70}Nb_{30}$, respectively. For agglomerates there is not a clear tendency, being their sizes between 50-200 μm for both alloys when they are present.

3.4. Mössbauer spectroscopy results

Figure 7 shows the evolution of the room temperature Mössbauer spectra with milling time. Two ferromagnetic sites were used to fit the residual α-Fe(X) phase: a sextet with hyperfine field, HF=33 T (no X atoms in the neighborhood), and another with HF=30.5 T (one X atom in the neighborhood). A quadrupolar distribution was used to describe the paramagnetic contributions, a priori assigned to the amorphous phase. Moreover, a distribution of hyperfine fields from 5 to 30 T was used to show the contribution from

the interface region and richer X neighborhoods. Figure 8 shows the fraction of the Fe

atoms contributing to each environment type. The fraction of the paramagnetic

contributions shows a continuous increase as milling time progresses.

Figure 9 shows the average isomer shift ($<IS>$) of the paramagnetic contributions as a

function of milling time for both studied alloys, either Zr or Nb play a similar role and

values of this parameter show a common behavior for the two alloys. Initially, for short

times of milling, for which hcp Zr and bcc Nb phases are detected by XRD, a reduction

of $<IS>$ from 0 to ~ -0.18 mm/s is observed. Values show a common behavior for both

alloys after the peaks attributed to the hcp Zr or bcc Nb phase in XRD patterns

disappear. After further milling, $<IS>$ reaches a stable value ~ -0.15 mm/s for both

samples. The values obtained for the $Fe_{70}Zr_{30}$ alloy agree with those reported for the

amorphous alloys $Fe_{65}Zr_{35}$ ($\delta = -0.16$ mm/s) [20] and $Fe_{70}Zr_{30}$ ($\delta = -0.16$ mm/s)

[16], but slightly higher values were reported for $Fe_{73}Zr_{27}$ ($\delta = -0.13$ mm/s) [21] and

Fe_2Zr ($\delta = -0.13$ mm/s) [10]. The values obtained for the $Fe_{70}Nb_{30}$ alloy also agree

with those reported for the amorphous alloy with the same composition ($\delta = -0.16$

mm/s) [16] and $Fe_{80}Nb_{20}$ ($\delta = -0.17$ mm/s) [14]. However, Eskandarany et al.

observed an isomer shift $\delta = -0.19$ mm/s in amorphous samples of $Fe_{52}Nb_{48}$ prepared

by mechanical alloying [22]. In fact, the slightly increase in $<IS>$ from the observed

minimum could be ascribed to the Fe enrichment of the amorphous phase as milling

progresses.

The quadrupole splitting distributions, $P(QS)$, are shown in figure 10. It shows the same

behavior for both alloys, with a non-zero probability for QS=0 mm/s. They also present

two well resolved maxima for short times of milling (t <6 and t <10 h for the $Fe_{70}Zr_{30}$

and $Fe_{70}Nb_{30}$ alloy, respectively) that become only one with the increase of milling

time. The first peak ($QS \sim 0.25$ mm/s) may be ascribed to Fe atoms in environments similar to Fe_2X. This environment, for X=Zr has QS=0.35 mm/s ($\delta = -0.13$ mm/s) [10] and for X=Nb has QS=0.34 mm/s ($\delta = -0.19$ mm/s) [24]. The second maximum found at low milling times ($QS \sim 1.25$ mm/s) may be attributed to X richer environments, e.g. Vincze et al. [28] reported QS=0.91 mm/s for $FeZr_3$. With these data, we can admit that QS distributions for low milling times do not really correspond to amorphous phase, but to Fe present in Zr and Nb remaining crystals (the times at which this two-peak $P(QS)$ are observed are in agreement with the observation of bcc Nb and hcp Zr phases by XRD). For larger milling times, a value of $<QS>$=0.53±0.07 mm/s is obtained for both alloys. This value is close to the values previously reported for $Fe_{70}Zr_{30}$ ($<QS>$=0.44 mm/s) and for $Fe_{70}Nb_{30}$ ($<QS>$=0.42 mm/s) [16].

Taking into account the nanocrystalline microstructure of our samples, some words on superparamagnetism are needed. An ensemble of magnetic nanoparticles shows superparamagnetic behavior above a certain temperature: the blocking temperature T_B. This temperature is defined as the temperature at which the relaxation time τ equals the experiment timescale τ_m [29]:

$$T_B = \frac{\Delta E}{k_B ln\left(\frac{\tau_m}{\tau_0}\right)} \tag{2}$$

where ΔE is the energy barrier that the magnetization flip has to overcome by thermal energy and can be considered to be proportional to the magnetic anisotropy constant K and particle volume V ($\Delta E = KV$), k_B is the Boltzmann constant and τ_0 is the length of time characteristic of the probed material. Although superparamagnetism should be expected for quasistatic measurements ($\tau_m \sim 100$ s) above Curie temperature T_C of the amorphous phase, it is worth noting that in Mössbauer spectroscopy $\tau_m \sim \tau_0$. Moreover,

the interaction between particles increases T_B [30]. These reasons are responsible for the absence of superparamagnetism in our samples.

3.5. Combination of Mössbauer spectroscopy and X-ray diffraction results

The composition of the core of nanocrystals have been estimated using the ratio between contributions at 30.5 T and 33 T, corresponding to $n =1$ and $n =0$, respectively, being n the number of Zr or Nb atoms in the two first shells surrounding the Fe probe. It has to be taken into account that the explored set is formed by 15 atoms, one of which is necessarily Fe. Therefore, the concentration of element X, $C(X)$, in a set of 14 atoms forming the two first shells that surround a Fe probe atom is [19]:

$$C(X) = \frac{15\, C(X)^W}{14} \tag{3}$$

where $C(X)^W$ is the concentration of element X in the whole system. Considering a binomial distribution, the probability to find a Fe environment with n X atoms can be determined as:

$$P(n) = \frac{14!}{(14-n)!n!}(C(X))^n(1 - C(X))^{14-n} \tag{4}$$

Therefore, the values of $C(X)^W$ (figure 11) can be obtained from the ratio between $P(0)$ and $P(1)$ as:

$$\frac{P(0)}{P(1)} = \frac{1-C(X)}{14C(X)} \tag{5}$$

which leads to:

$$C(X)^W = \frac{14}{15}\frac{P(1)}{14P(0)+P(1)} \tag{6}$$

For the $Fe_{70}Nb_{30}$ alloy, the results are shown along with the values obtained from the lattice parameter evolution using Vegard's law and considering $a=2.8665$ and 3.3022 Å for pure bcc Fe and bcc Nb, respectively. Noting that Vegard's law is just an estimation,

both plots are in good agreement. For both alloys, the values obtained (about 3 and 5 at. %, for Zr and Nb containing alloys, respectively), are well below the nominal one, 30 at. %. This indicates that the composition of the amorphous phase is progressively enriched in Fe as bcc-Fe phase fraction decreases, in agreement with the evolution of the position of the amorphous halo which indicated a decrease in the metal-metal distance as milling progresses. As the amorphous phase becomes enriched in Fe (the smallest atom in our study) the interatomic distances decrease (see figure 4(b)).

Once we know the compositions of each phase, we can compare the XRD and MS data. The correlation between the values of amorphous fraction calculated from XRD and paramagnetic contributions from Mössbauer spectra is shown in figure 12(a). Paramagnetic contributions from MS are detected earlier than amorphous phase from XRD. Although from XRD no crystalline phase is detected after larger milling times, from Mössbauer data the maximum amorphous phase reaches 97% and 95% for the $Fe_{70}Zr_{30}$ and $Fe_{70}Nb_{30}$, respectively, in agreement with some works in the literature [2] that show that the amorphous fraction could not reach 100% due to recrystallization phenomena. However, it is worth noting that the data obtained from both techniques do not refer to the same observable; XRD data correspond to the amount of phase weighted by their scattering power, while Mössbauer spectroscopy measures the fraction of the total number of Fe atoms in a common environment. In order to compare the XRD and Mössbauer data, it would be necessary to correct the diffraction areas with the scattering power of each phase for XRD and to take into account the composition of each phase to correct the fraction of Fe atoms for Mössbauer spectroscopy. This analysis is shown in figure 12(b). For $X > 15\%$, the correlation between both measurements is good and follows a linear trend. The comparison of the values obtained for the evolution of amorphous phase from both techniques permits us to affirm that MS is a more sensitive

technique than XRD in order to detect small phase fractions, where paramagnetic and

ferromagnetic phases coexist.

Moreover, from the area ratio between the contribution of the hyperfine field

distribution (interface region) to ferromagnetic sites contribution (crystalline core

region), interface thickness can be estimated as:

$$\frac{Area_{int}}{Area_{cryst}} = \frac{4\pi R^2 \delta}{^4/_3 \pi R^3} \tag{7}$$

where $Area_{int}$ and $Area_{cryst}$ are the areas of the interface and crystalline regions,

respectively, and δ is the interface thickness. As a first approximation, $Area_{int}$ could be

identified as HFD contribution and $Area_{cryst}$ could be identified as the sum of 33 T and

30.5 T contributions. However, as we already estimated the X content in the bcc-Fe

crystals we can refine the expression (7) taking into account that crystalline

environments with more than one X atom in the neighborhood will contribute to HFD.

Therefore, expression (7) should be corrected to:

$$\frac{Area_{int}}{Area_{cryst}} = \frac{A_{HFD} - A_{P(n>1)}}{A_{P(0)} + A_{P(1)} + A_{P(n>1)}} = \frac{4\pi R^2 \delta}{^4/_3 \pi R^3} \tag{8}$$

where $A_{P(i)}$ is the Mössbauer area corresponding to the i contribution (e.g. for 3 at. % of

Zr in bcc-Fe, $A_{P(0)} = 63.3$ %, $A_{P(1)} = 29.4$ % and thus $A_{P(n>1)} = 7.3$ %). Therefore:

$$Area_{cryst} = \left(A_{P(0)} + A_{P(1)}\right)\frac{100}{P(0) + P(1)} \tag{9}$$

and:

$$Area_{int} = A_{HFD} - \left(A_{P(0)} + A_{P(1)}\right)\frac{100 - P(0) - P(1)}{P(0) + P(1)} \tag{10}$$

So, finally, equation (8) could be rewritten as:

$$3\frac{\delta}{R} = \frac{A_{HFD} - \left(A_{P(0)} + A_{P(1)}\right)\frac{100 - P(0) - P(1)}{P(0) + P(1)}}{\left(A_{P(0)} + A_{P(1)}\right)\frac{100}{P(0) + P(1)}} \tag{11}$$

12

Figure 13 shows the evolution of R/δ as a function of milling time for both alloys. From the inverse of slope of R/δ vs crystal size D obtained from XRD data it is possible to estimate δ. This analysis was applied to our alloys (inset figure 13), obtaining a value of interface thickness $\delta = 0.43 \pm 0.07$ nm. Similar results can be found in the literature [31, 32].

4. Conclusions

High energy ball milling allows amorphous Fe-Zr and Fe-Nb alloys with 70 at. % Fe content to be successfully prepared. The composition of nanocrystals of bcc Fe-based supersaturated solution is obtained through a systematic analysis of the relationship of Mössbauer data with microstructural parameters from X-ray diffraction data. For short milling times, the quadrupole distribution of Mössbauer spectra is consistent with the existence of two kinds of environment, Fe-rich environments and X-rich (X=Zr, Nb) environments ascribed to Fe atoms in the remnant X crystals. For larger milling times, X-ray patterns clearly provide evidence for amorphous phase, which is observed by Mössbauer spectroscopy as a single peak. From the ratio between high hyperfine field contributions, composition of the nanocrystal is estimated to saturate around 3 at %. Zr and 5 at. % Nb for $Fe_{70}Zr_{30}$ and $Fe_{70}Nb_{30}$, respectively. From the evolution of the compositions of the core of nanocrystals it has been possible to estimate the interface thickness, $\delta = 0.43 \pm 0.07$ nm. Finally, the comparison between Mössbauer spectroscopy and X-ray diffraction indicates that the first one is a more sensitive technique to detect small phase fractions where paramagnetic and ferromagnetic phases coexist.

13

References

[1] Bloor D, Brook RJ, Flemngis MC, Mahajan S. The encyclopedia of advanced materials: Oxford: Pergamon Press; 1994.

[2] Suryanarayana C. Mechanical alloying and milling. Progress in Materials Science 2001;46:1-184 https://doi.org/10.1016/S0079-6425(99)00010-9

[3] Pappas D. Status and potential of atmospheric plasma processing of materials. Journal of Vacuum Science & Technology A 2011;29: 020801 https://doi.org/10.1116/1.3559547

[4] Lavernia EJ, Srivatsan TS. The rapid solidification processing of materials: science, principles, technology, advances, and applications. Journal of Materials Science 2010;45:287-325 https://doi.org/10.1007/s10853-009-3995-5

[5] Benjamin JS, Volin TE. The mechanism of mechanical alloying. Metallurgical Transactions 1974;5:1929-34 https://doi.org/10.1007/BF02644161

[6] Blazquez JS, Ipus JJ, Lozano-Perez S, Conde A. Metastable Soft Magnetic Materials Produced by Mechanical Alloying: Analysis Using an Equivalent Time Approach. Jom 2013;65:870-82 https://doi.org/10.1007/s11837-013-0616-1

[7] Gütlich P, Bill E, Trautwein AX. Mössbauer Spectroscopy and Transition Metal Chemistry: Springer; 2011.

[8] Altounian Z, Stromolsen JO. SUPERCONDUCTIVITY AND SPIN FLUCTUATIONS IN CU-ZR,NI-ZR,CO-ZR AND FE-ZR METALLIC GLASSES. Physical Review B 1983;27:4149-56 https://doi.org/10.1103/PhysRevB.27.4149

[9] Mishra D, Perumal A, Srinivasan A. Magnetic properties of mechanically alloyed Fe(100-x)Zr(x) (20 <= x <= 35) powder. Journal of Physics D-Applied Physics 2008;41 https://doi.org/10.1088/0022-3727/41/21/215003

[10] Concas G, Congiu F, Spano G, Bionducci M. Investigation of the ferromagnetic order in crystalline and amorphous Fe2Zr alloys. Journal of Magnetism and Magnetic Materials 2004;279:421-8 https://doi.org/10.1016/j.jmmm.2004.02.012

[11] Unruh KM, Chien CL. MAGNETIC-PROPERTIES AND HYPERFINE INTERACTIONS IN AMORPHOUS FE-ZR ALLOYS. Physical Review B 1984;30:4968-74 https://doi.org/10.1103/PhysRevB.30.4968

[12] Voss S, Palm M, Stein F, Raabe D. Phase Equilibria in the Fe-Nb System. Journal of Phase Equilibria and Diffusion 2011;32:97-104 https://doi.org/10.1007/s11669-010-9808-3

[13] Jartych E, Oleszak D, Zurawicz JK. Hyperfine interactions in amorphous Fe-Nb alloys prepared by mechanical alloying. Hyperfine Interactions 2001;136:25-33 https://doi.org/10.1023/A:1015550913839

[14] Povstugar IV, Yelsukov EP, Zhernovenkova YV, Butyagin PY. Initial stage of mechanical alloying in Fe(80)X(20) (X = Nb, Ta) systems. Colloid Journal 2004;66:197-203 https://doi.org/10.1023/B:COLL.0000023121.03238.e8

[15] Blachowski A, Ruebenbauer K, Zukrowski J. Influence of niobium impurity on spin density in metallic iron. Physica Status Solidi B-Basic Solid State Physics 2005;242:3201-8 https://doi.org/10.1002/pssb.200541086

[16] Blazquez JS, Ipus JJ, Conde CF, Conde A. Comparison of equivalent ball milling processes on Fe70Zr30 and Fe70Nb30. Journal of Alloys and Compounds 2012;536:S9-S12 https://doi.org/10.1016/j.jallcom.2011.11.084

[17] Ipus JJ, Blazquez JS, Franco V, Millan M, Conde A, Oleszak D, et al. An equivalent time approach for scaling the mechanical alloying processes. Intermetallics 2008;16:470-8 https://doi.org/10.1016/j.intermet.2007.12.011

[18] Balogh J, Bujdoso L, Kaptas D, Kemeny T, Vincze I, Szabo S, et al. Mossbauer study of the interface of iron nanocrystallites. Physical Review B 2000;61:4109-16 https://doi.org/10.1103/PhysRevB.61.4109

[19] Blázquez JS, Ipus JJ, Franco V, Conde CF, Conde A. Extracting the composition of nanocrystals of mechanically alloyed systems using Mossbauer spectroscopy. Journal of Alloys and Compounds 2014;610:92-9 https://doi.org/10.1016/j.jallcom.2014.04.195

[20] Pizarro R, Garitaonandia JS, Plazaola F, Barandiaran JM, Greneche JM. Magnetic and Mossbauer study of multiphase Fe-Zr amorphous powders obtained by high energy ball milling. Journal of Physics-Condensed Matter 2000;12:3101-12 https://doi.org/10.1088/0953-8984/12/13/318/

[21] Povstugar IV, Butyagin PY, Dorofeev GA, Elsukov EP. Kinetics of the initial stage of mechanical alloying in the Fe(80)Zr(20) system. Colloid Journal 2002;64:178-85 https://doi.org/10.1023/A:1015248810332

[22] El-Eskandarany MS, Bahgat AA, Gomaa NS, Eissa NA. Kinetics and formation mechanism of amorphous Fe52Nb48 alloy powder fabricated by mechanical alloying. Journal of Alloys and Compounds 1999;290:181-90 https://doi.org/10.1016/S0925-8388(99)00222-4

[23] Velez GY, Alcazar GAP, Zamora LE. Influence of atomic ordering on the Fe2Nb antiferromagnetic alloy. Journal of Magnetism and Magnetic Materials 2014;354:333-5 https://doi.org/10.1016/j.jmmm.2013.11.031

[24] Velez GY, Alcazar GAP, Zamora LE, Tabares JA. Structural and Magnetic Study of the Fe2Nb Alloy Obtained by Mechanical Alloying and Sintering. Journal of Superconductivity and Novel Magnetism 2014;27:1279-83 https://doi.org/10.1007/s10948-013-2428-5

[25] Brand RA, Lauer J, Herlach DM. The evaluation of hyperfine field distribuions in overlapping and asymmetric Mossbauer spectra: A study of the amorphous alloy PD77.5-XCu6Si16.5FeX. Journal of Physics F-Metal Physics 1983;13:675-83 https://doi.org/10.1088/0305-4608/13/3/018

[26] Egami T. Rapidly Solidified Alloys: Processes, Structures, Properties, Applications. New York: Marcel Dekker, Inc.; 1993.

[27] Zarubova N, Moser N, Kronmuller H. KINETICS OF CRYSTALLIZATION IN A FE90ZR10 AMORPHOUS ALLOY. Materials Science and Engineering a-Structural Materials Properties Microstructure and Processing 1992;151:205-15 https://doi.org/10.1016/0921-5093(92)90209-J

[28] Vincze I, Vanderwoude F, Scott MG. Local structure of amorphous Zr3Fe. Solid State Communications 1981;37:567-70 https://doi.org/10.1016/0038-1098(81)90135-6

[29] Morup S, Hansen MF. Handbook of Magnetism and Advanced Magnetic Materials: John Wiley & Sons; 2007.

[30] Franco V, Blazquez JS, Conde CF, Conde A, Kiss LF, Kemeny T, et al. Frequency dependence of the superparamagnetic transition in a Finemet-type nanocrystalline alloy. Physica Status Solidi a-Applied Research 2004;201:3314-8 https://doi.org/10.1002/pssa.200405471

[31] Blazquez JS, Franco V, Conde CF, Conde A, Ferenc J, Kulik T. High temperature coercivity of Nb-containing HITPERM alloys: Effect of Cu addition. Materials Letters 2008;62:780-3 https://doi.org/10.1016/j.matlet.2007.06.067

[32] Alleg S, Hamouda A, Azzaza S, Bensalem R, Sunol JJ, Greneche JM. Solid state amorphization transformation in the mechanically alloyed Fe27.9Nb2.2B69.9 powders. Materials Chemistry and Physics 2010;122:35-40 https://doi.org/10.1016/j.matchemphys.2010.03.006
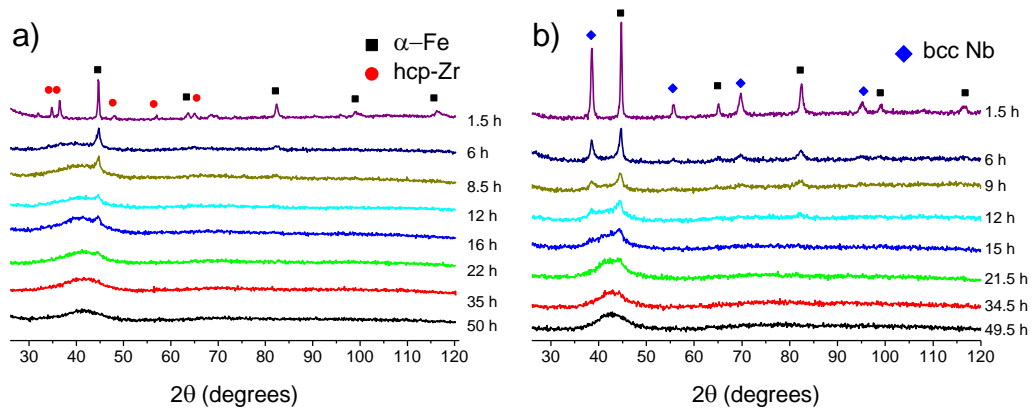
FIGURES

Figure 1. XRD patterns of the amorphous samples after milling up to different times for a) $Fe_{70}Zr_{30}$ and b) $Fe_{70}Nb_{30}$.
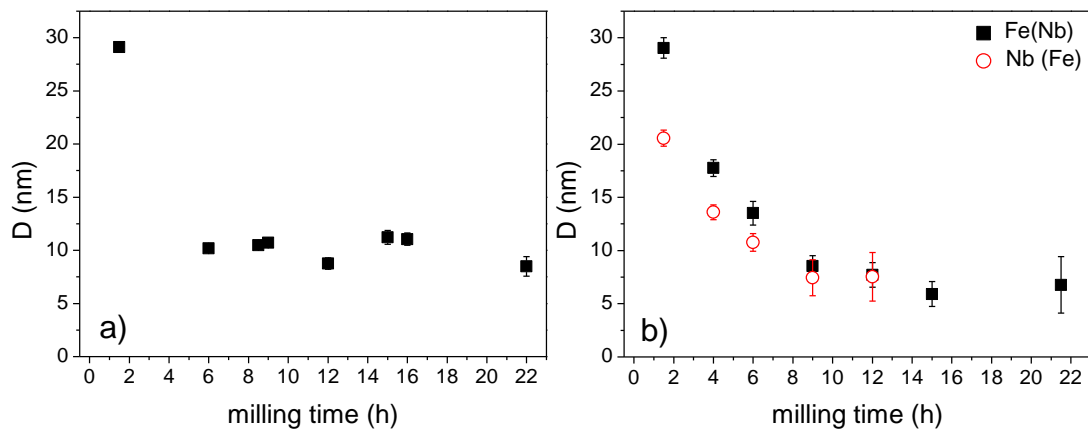

Figure 2. Evolution of crystal size of the a) Fe(Zr) and b) Fe(Nb) and Nb(Fe) (right) bcc phases as a function of milling time.
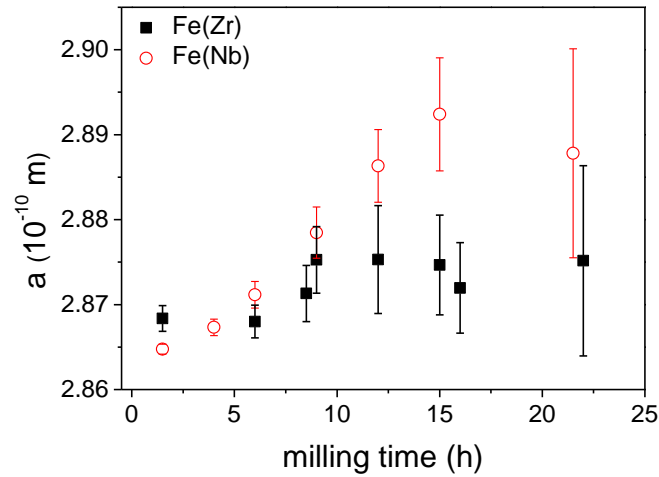
Figure 3. Evolution of lattice parameter of the Fe(Zr) and Fe(Nb) bcc phases as a function of milling time.
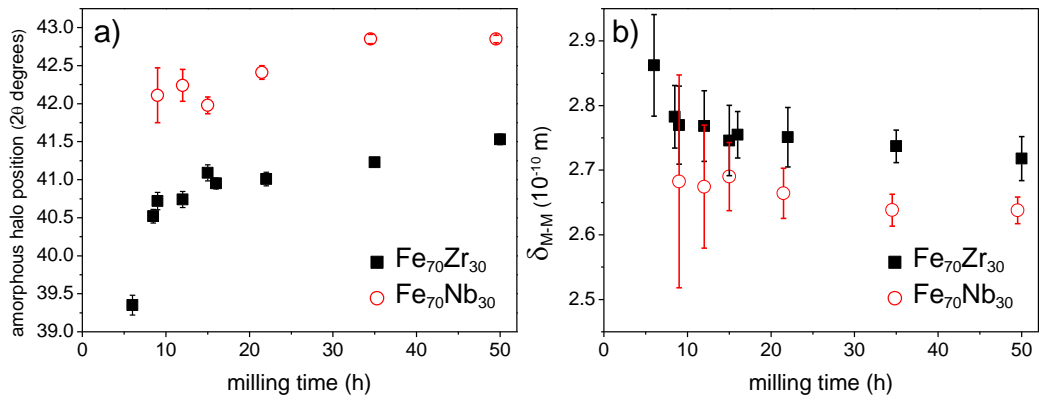

Figure 4. a) Evolution of the amorphous halo position and b) metal-metal distance as a function of milling time.
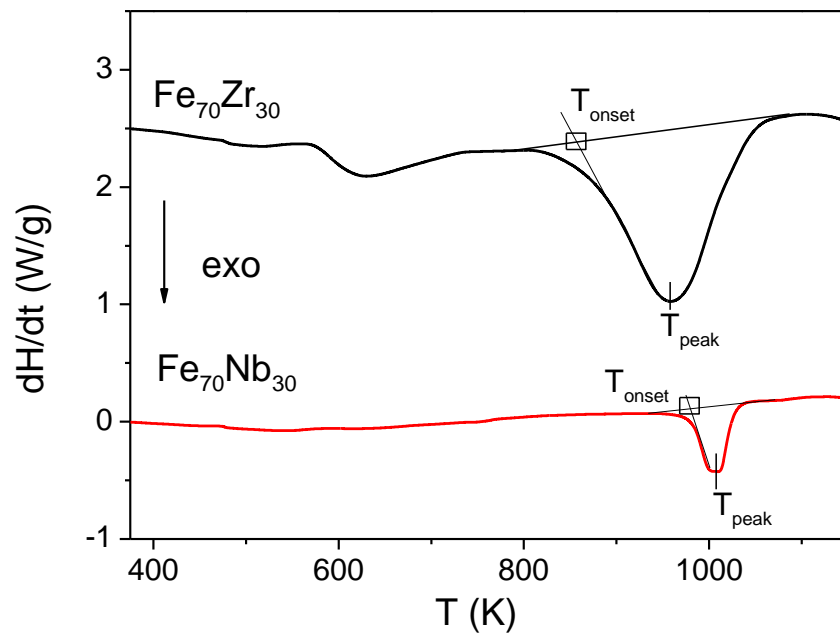
Figure 5. Non-isothermal DSC scans at 20 K/min for both studied samples after 50 h (Zr containing alloy) and 49.5 h (Nb containing alloy) of milling. Crystallization peak and onset temperatures are indicated.
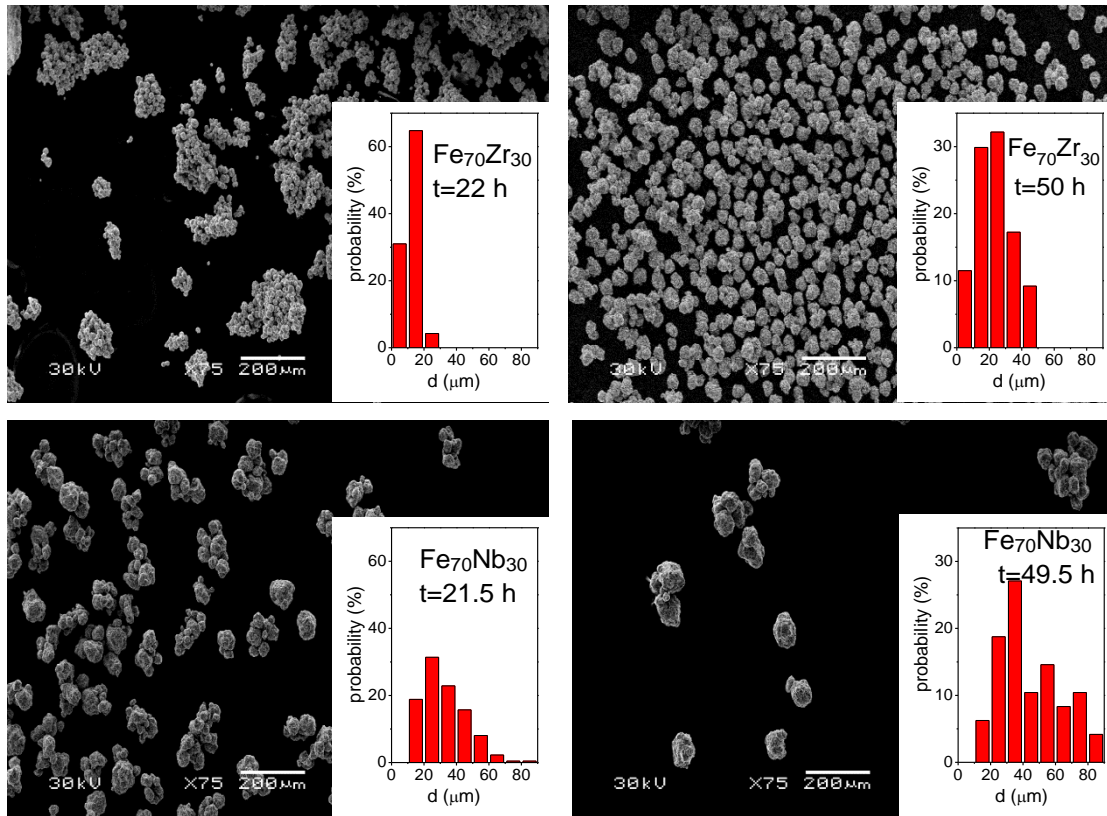
Figure 6. Scanning electron microscopy images in secondary electrons mode for the two studied alloys after selected milling times. Insets show the histograms for the powder particle size.
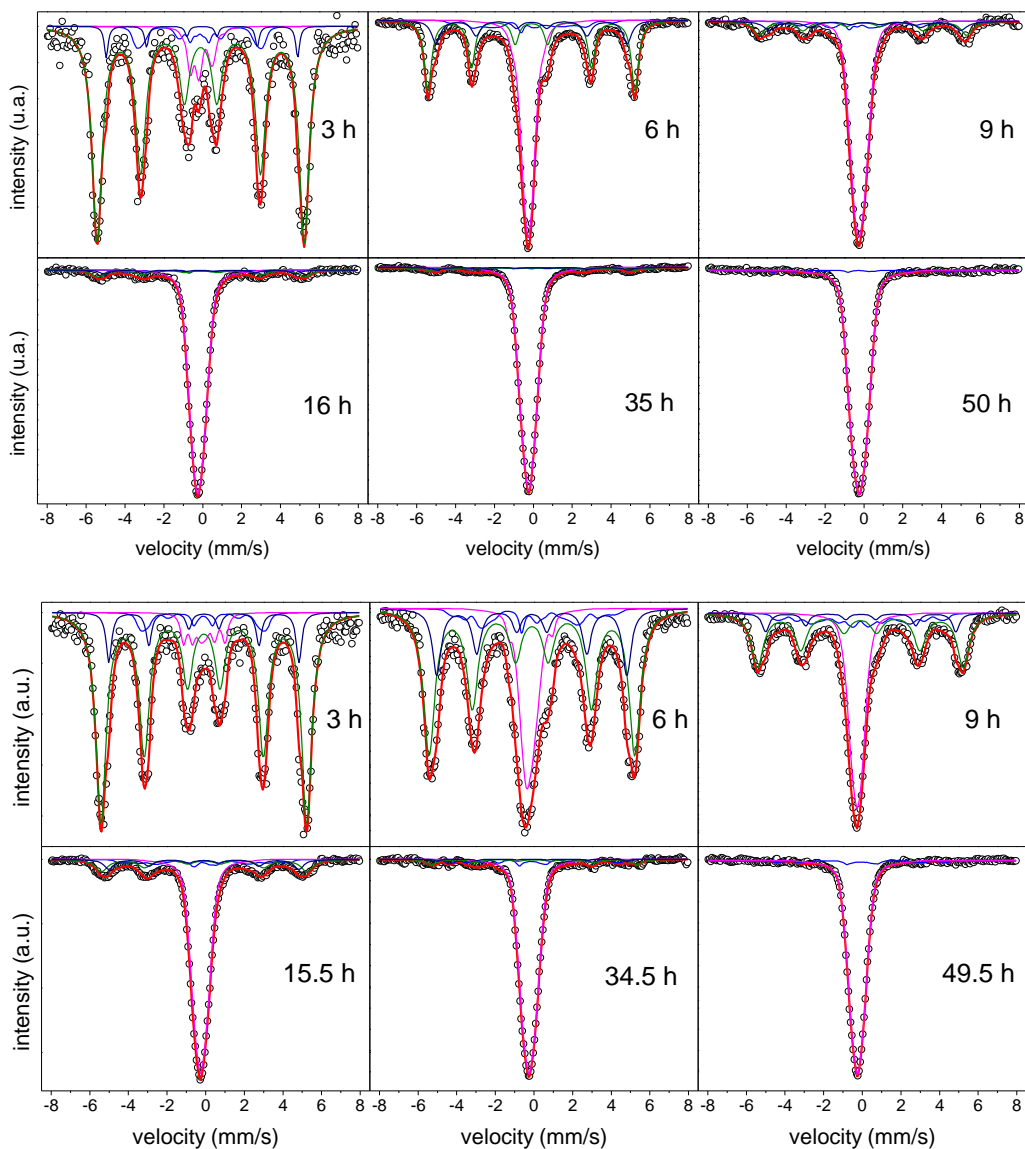
Figure 7. Experimental Mössbauer spectra (symbols) and model fitting (lines) for several milling times: $Fe_{70}Zr_{30}$ (up), $Fe_{70}Nb_{30}$ (down).
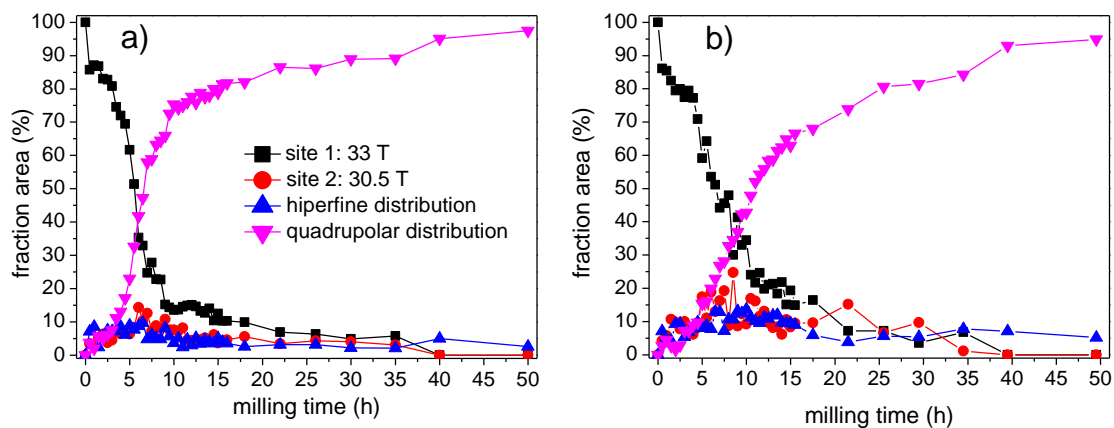
Figure 8. Phase contribution to Mössbauer spectra fitting for a) $Fe_{70}Zr_{30}$ and b) $Fe_{70}Nb_{30}$ alloys.
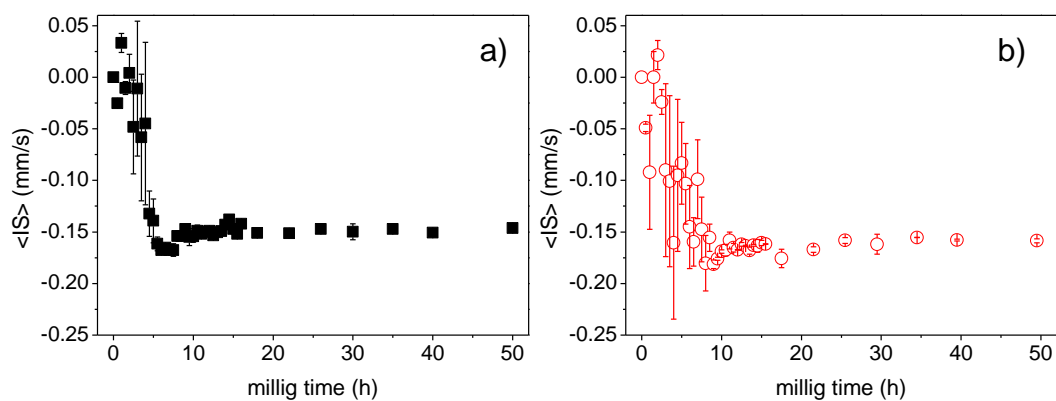
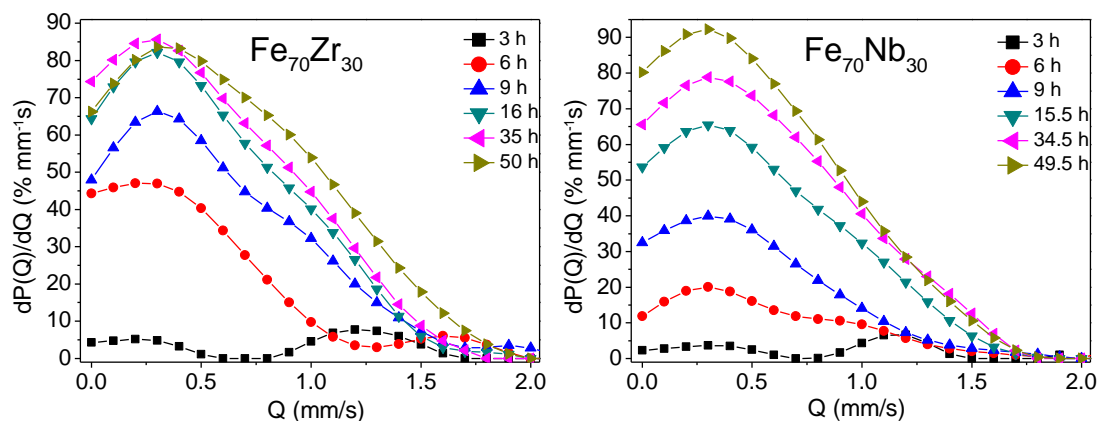Figure 9. Average isomer shift (<IS>) of paramagnetic contributions as a function of milling time for a) $Fe_{70}Zr_{30}$ and b) $Fe_{70}Nb_{30}$ alloys.

Figure 10. Probability distribution of quadrupole splitting for both samples after several milling times.
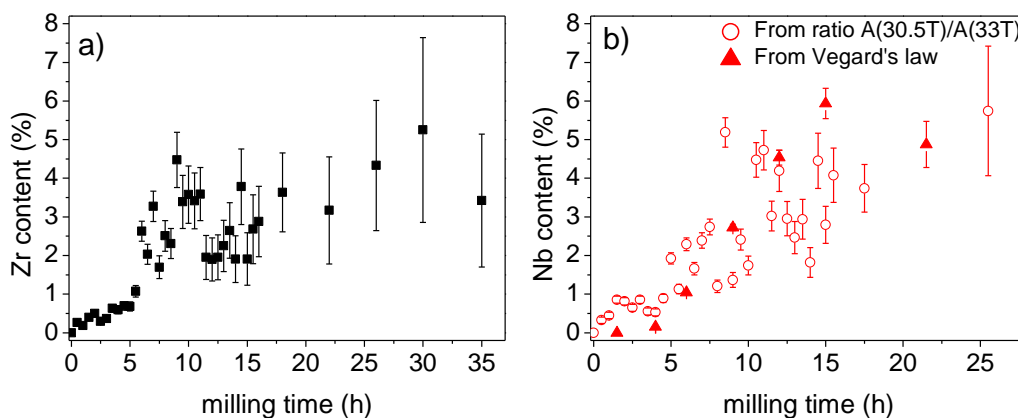

Figure 11. a) Content of Zr inside the nanocrystals from Mössbauer results and b) content of Nb inside the nanocrystals from Mössbauer results and Vegard's law.
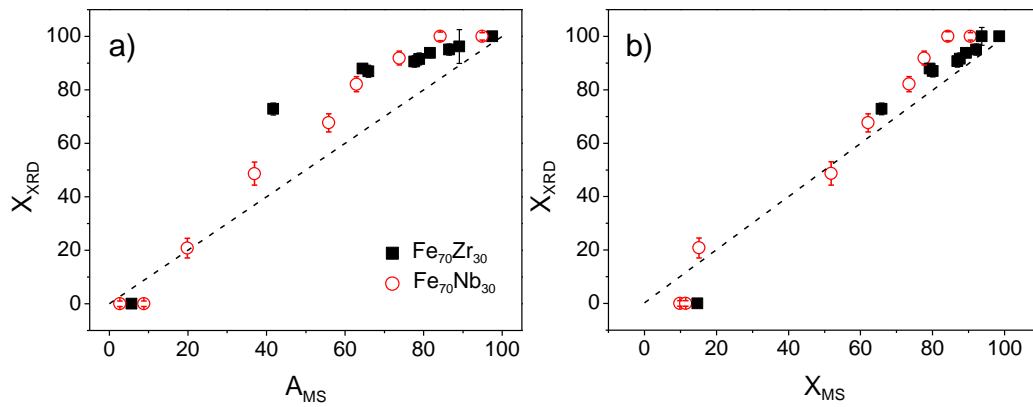
Figure 12. Amorphous fraction from XRD patterns as a function of a) the relative area of paramagnetic contribution and b) the estimated amorphous phase fraction from Mössbauer spectra. The dashed lines correspond to the identity line.
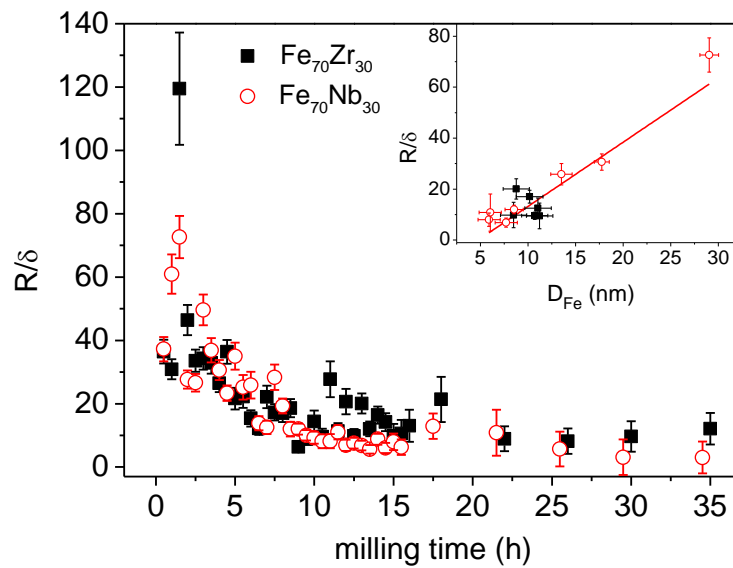

Figure 13. Evolution of R/δ as a function of milling time for both alloys. Inset shows the relation between R/δ and D_{Fe} obtained from XRD data.

Table 1. Crystallization temperature of studied alloys after 50 h (Zr containing alloy) and 49.5 h (Nb containing alloy) of milling, respectively

Sample	T_{onset} (K)	T_{peak} (K)
$Fe_{70}Zr_{30}$	862	956
$Fe_{70}Nb_{30}$	980	1006